

Multidopant Induced Entropy Effect on $\text{TiS}_2/\text{TiSe}_2$ -Based Layered Anode and Formation of Electrode–Electrolyte Interphase

Amreen Bano* and Dan T. Major

Van der Waals (vdW) heterostructures (HSs) have attracted intense interest worldwide as they offer several routes to design materials with novel features and wide-ranging applications. Unfortunately, vdW HSs are currently restricted to a small number of stackable layers due to the weak vdW forces holding adjacent layers together. In this article, computational studies of a bulk vdW material consisting of alternating TiS_2 and TiSe_2 (TSS) vertically arranged layers are reported as a potential candidate for anode applications. Density functional theory (DFT) calculations and ab-initio molecular dynamics (AIMD) simulations are used to explore the effect of close-to-high entropy on several electrochemically relevant properties of the bulk HS (TSS-HS)

by substituting Mo_{5+} and Al_{3+} at the transition metal site (Ti_{4+}). Additionally, solvation shell formation at the electrode–electrolyte interphase (EEI) is studied using AIMD to determine Li-coordination. Based on the properties computed using DFT and AIMD, ‘entropy-induced’ TSS-HS (TSS-EI) might possess improved electrochemical performance over standard TSS-HS. Factors that can improve the performance of TSS-EI are 1) less structural deformation, 2) strong bonding (metal-sulphur), 3) better electron mobility, 4) wider operational voltage window, and 5) faster Li-ion diffusion. Observations suggest that ‘entropy’ can be an effective strategy to design new anode materials for Li-ion batteries.

1. Introduction

Owing to their high energy density, low cost, large storage capacity and cycling stability, lithium-ion batteries (LIBs) have gained tremendous attention as electronic energy storage devices.^[1–4] Since the discovery of graphene, with its high electroconductivity and specific surface area, graphene-based anode materials have been studied extensively.^[5] However, poor mechanical stability and low specific capacity^[6] are some limiting factors which are difficult to overcome, prompting researchers to look for improved or alternative anode materials. These strategies include doping,^[7,8] strain,^[9,10] defects,^[11,12] or heterostructures (HSs) with different layered materials.^[5,13] In this regard, HSs are an attractive alternative that have already shown good promise. The distinct layers of HSs are held together by interlayer van der Waals (vdW) interactions. These HSs not only exhibit new basic physics^[14,15]

but also have shown considerable performance in applications, such as field-effect transistors^[13,16,17] and photodetectors.^[18–20] Additionally, there is a plethora of literature focusing on the virtues of graphene-like HSs used as electrode materials.^[21–23] Some promising postgraphene candidates are transition metal dichalcogenides (TMDs),^[24–27] phosphorene,^[28] and silicene.^[29] The layered TMD materials not only have properties similar to graphene but also they have many mechanical, optical, chemical, thermal, and electrical capabilities that are comparable to or superior to graphene.^[27,30,31] The weak interlayer dispersion interactions in TMDs or their HSs facilitate intercalation of foreign atoms (such as Li-ions) which is reported to improve the electron conductivity of the material.^[32] Hence, layered TMDs and their HSs have previously been proposed as promising anode materials for LIBs.^[33,34]

Commonly, a vdW HS is prepared by mechanically stacking one 2D layer on top of another. Interestingly, some bulk vdW HSs exist in nature, like Frankencite, which is a naturally occurring vdW HS composed of SnS_2 and PbS layers stacked alternately.^[35] There are few examples of such bulk vdW HSs, and synthesizing such HSs remains difficult despite the advancements in 2D materials research. Another example of a bulk vdW HS is the 6 R-phase of TaS_2 , which consists of alternating layers of 1 H-(superconducting)^[36,37] and 1 T- TaS_2 (Mott insulator).^[38] Two typical layered TMD materials, TiS_2 and TiSe_2 , have gained traction as potential anode materials.^[39–43]

The performance of HSs as anode materials has been studied extensively for materials like MoS_2/WS_2 ,^[44] $\text{WS}_2/\text{NbSe}_2$,^[45] and $\text{NiSe}_2/\text{SnSe}_2$.^[46] Still, to increase the choice of possible anode materials, it is desirable to go beyond these base materials and pursue more complex materials. Considering the difficulty

A. Bano

Research Institute for Sustainable Energy (RISE)

TCG Centres for Research and Education in Science and Technology (TCG-CREST)

Kolkata 700091, India

E-mail: amreen.bano@tcgcrest.org

A. Bano

Academy of Scientific and Innovative Research (AcSIR)

Ghaziabad 201002, India

A. Bano, D. T. Major

Department of Chemistry, Israel National Institute of Energy Storage (INIES) and Institute for Nanotechnology & Advanced Materials Bar-Ilan University

Ramat-Gan 5290002, Israel



Supporting information for this article is available on the WWW under <https://doi.org/10.1002/batt.202500299>

in synthesizing HSs, it is of value to first consider potential materials in silico. Here, we focus on the HSs with '*close-to-high entropy*' elemental configuration. The study of high entropy battery materials commenced with the development of high entropy metal oxides as LIB and other action ion based anodes that showed significant improvement in specific capacity and capacity retention.^[47–52,53] This direction was further expanded to high entropy Li-ion cathodes that showed improved electrochemical performance.^[54,55] We note that the terms '*high entropy*', '*compositionally complex*' and '*multicomponent*' are not necessarily interchangeable. Under ideal mixing conditions, where components are randomly distributed, the configurational entropy is expressed as^[56]

$$S_{\text{Config}}^{\text{ideal}} = -k_B \sum_{i=1}^N x_i \ln x_i \quad (1)$$

where x_i indicates the mole fraction of component i on the site of mixing and k_B is the Boltzmann constant. To be considered high entropy, a material must have an $S_{\text{Config}}^{\text{ideal}}$ value of $\geq 1.5R$.^[57] For instance, the traditional cathode material $\text{LiNi}_{0.5}\text{Mn}_{0.3}\text{Co}_{0.2}\text{O}_2$, has an $S_{\text{Config}}^{\text{ideal}}$ of $1.03k_B$ per transition metal, and therefore, cannot be considered a '*high entropy*' material.^[58] High-entropy materials can produce a large ensemble of local environments instead of the formation of local homogenous domains with clusters of like atoms which can form in low-entropy materials. Studies have indicated that multiensemble local environments might reduce the short-range ordering, which is one of the causes of impaired electrochemical performance. Reduced short-range ordering enables '*high entropy*' materials to attain higher rates and capacities.^[55,59] In addition, compared to low-entropy materials, high-entropy materials show a greater tolerance for lattice distortions, allowing for significant changes to the energy landscape for ion diffusion. As recently demonstrated in high-entropy oxide-based materials, carefully designed lattice distortions can produce percolating diffusion routes, allowing orders of magnitude increase in ionic conductivities.^[60] Furthermore, the effect of high entropy has also been explored in electrolytes where ion (e.g., Li/Na) transport improved when multiple anion additives were added to the electrolyte.^[53,61–64]

It is important to mention that experimentally achieving stable high-entropy phases remains a significant challenge due to issues such as phase segregation, dopant clustering, and synthesis-induced defects.^[65,66] Techniques like dealloying,^[67–69] low-temperature liquid-phase method (also known as the solvent thermal method),^[70,71] constraint-assisted spark plasma sintering,^[72] carbon thermal shock, and so on.^[73,74] require precise control to ensure homogeneous dopant distribution without compromising structural integrity. In graphite and other carbon-based anodes, introducing multiple heteroatoms often leads to localized inhomogeneities and unpredictable electrochemical behavior.^[75] These limitations underscore the importance of computational methods, which offer atomistic insights into dopant effects, diffusion pathways, and solvation structures prior to laborious synthesis.

In this work, we studied the effect of *close-to-high* entropy on structural, electronic, bond strength, and electrochemical

characteristics of a typical bulk HS anode TSS-HS using Density functional theory (DFT) and ab-initio molecular dynamics (AIMD) calculations. Additionally, we explored Li-ion diffusion at the anode–electrolyte interphase. Our computational analysis suggests the synergistic effects of entropy stabilization and aliovalent doping result in reduced volume expansion, enhanced Li^+ diffusion, and increased electronic conductivity due to Mo-derived states at the Fermi level. These contributions address key challenges in LIB anode design, including structural degradation and sluggish ion transport.

2. Computational Methods

Using DFT, we performed high-throughput calculations on pristine and close-to-high entropy 1T-TiS₂-TiSe₂ (TSS) bulk HS to explore its potential as a layered anode material for Li-ion batteries. To meet the '*close-to-high entropy*' criteria, that is, $N \geq 5$, we substitute Mo⁵⁺ and Al³⁺ at the transition metal site (Ti). The choice of substituent elements (Mo and Al) are based on their contribution in strong O-bonding in layered NCM based cathode materials as well as reduced structural deformation during charging.^[54,76,77] Similarly, Sulphur and Selenium form relatively strong bonds with the transition metals Mo^[78–80] and Al,^[81,82] and hence, these were considered for '*close-to-high entropy*' anodes. Several Ti-substitution sites were explored using DFT to find suitable spots for Mo and Al in TSS-HS. Using Equation (1), we obtained $S_{\text{Config}}^{\text{ideal}} = 1.44k_B$ per component for our TSS-EI anode model, which is significantly close to the ideal high entropy limit, that is, '*close-to-high entropy*'. The optimized TSS-HS and entropy-induced TSS (TSS-EI) are shown in Figure 1a,b. A supercell of $3 \times 3 \times 2$ was used to build the TSS-HS and TSS-EI models. All DFT calculations used the Vienna ab initio simulation package (VASP).^[83,84] For all computations, projector augmented wave potentials^[85] were utilized. The electron-exchange correlation term was treated using the Perdew, Burke, and Ernzerhof (PBE) functional, which is based on the generalized gradient approximation.^[86] We included

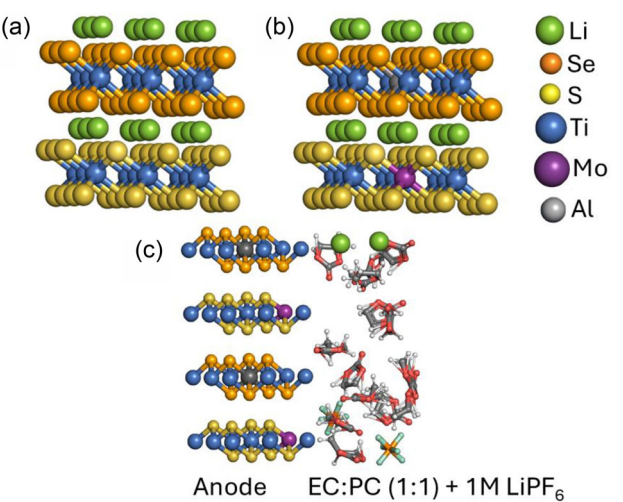


Figure 1. Optimized crystal structures of a) TSS-HS and b) TSS-EI. c) EEI obtained using Packmol.^[102]

onsite Coulomb interactions with Hubbard-*U* terms^[87] ($\text{PBE} + U$) for strongly correlated elements with *d*-orbitals, such as Ti and Mo. The effective *U* parameters for Ti and Mo used were 4.0^[88] and 5.0 eV^[76] respectively. Spin-polarized calculations were carried out with a $5 \times 5 \times 2$ *k-mesh*. Grimme's D3 dispersion correction^[89] was used to treat vdW interactions. For the analysis of delithiated states of TSS-HS and TSS-EI, Monte Carlo simulations were performed to identify the preferred Li-ion sites at various Li-concentrations (that is, for lithiated to fully delithiated states: 100.0, 87.5, 75.0, 67.5, 50.0, 32.5, 25.0, 12.5, 0.0). Using the Ising model, we generated 20 000 initial guess ground state magnetic configurations for the TSS-HS and TSS-EI systems for the DFT calculations. The lowest three of the 20 000 potential spin configurations were taken into consideration for DFT calculations. The lowest energy structure obtained using DFT was considered for final calculations and analysis. We found that TSS-HS prefers a ferromagnetic state, while TSS-EI prefers an antiferromagnetic state as the ground state magnetic ordering. For the plane-wave basis set, we employed a 520 eV kinetic energy cut-off. In geometry optimizations, the force per atom convergence criterion was 0.01 eV Å⁻¹, whereas the convergence criterion for self-consistent field electronic structure computations was 1×10^{-5} eV.

To determine the strength of metal-anion bonds at various Li-concentrations (metal = Ti, Mo, and Al; anion = S and Se), we performed partial crystal orbital Hamiltonian population (pCOHP) analysis using the LOBSTER package.^[90-93] Maximum bond distances between Ti—S/Se, Mo—S, and Al—Se were between 1–3 Å for the pCOHP calculations. This analysis provides clues regarding the 'high entropy' effect on structural deformation of the TSS under the effect of Li-extraction.

Furthermore, to obtain the voltage profile of Li-(de)intercalation of TSS-HS and TSS-EI, the following expression was used^[94-96]

$$V = -\frac{[E(\text{Li}_{x+dx}\text{TSS}) - E(\text{Li}_x\text{TSS})]}{dx} + E(\text{Li}_{bcc}) \quad (2)$$

Here, $E(\text{Li}_{x+dx}\text{TSS})$ and $E(\text{Li}_x\text{TSS})$ are the energies per formula unit of TSS-HS (or TSS-EI) at $x + dx$ and x Li-concentrations. $E(\text{Li}_{bcc})$ is the energy per formula unit of bulk Li metal.

We also explored the relative performance of TSS-HS and TSS-EI anode materials forming an interface with a basic, common electrolyte composed of EC:PC (1:1) organic solvent molecules with 1M LiPF₆ salt.^[97,98] To analyze the formation of a solid-electrolyte interphase (SEI) between the anode (TSS-HS/TSS-EI) and the electrolyte we used AIMD simulations as implemented in VASP^[83,84] at a temperature of 300 K. These simulations demand significant computational resources, and therefore, we used a reduced $3 \times 3 \times 2$ *k-mesh*.^[99] The canonical ensemble (NVT) with the Nose-Hoover thermostat as a heat bath was employed. A time step of 1.0 fs and a total of 6 ps simulation time were considered. The diffusion coefficient of Li-ions was determined using mean square displacement (MSD) as follows^[100,101]

$$\text{MSD}(t) = \langle [r(t) - r(0)^2] \rangle \quad (3)$$

Employing the Einstein formula, we obtain the diffusion coefficient as follows

$$D = \frac{1}{6} \frac{d \text{MSD}(t)}{dt} \quad (4)$$

We note that these equations are only approximate single particle diffusion equations rather than cooperative multi-ion diffusion equations. We used the Packmol software^[102] to create the optimized anode-electrolyte interphase. The EEI modeled via AIMD simulations is shown in Figure 1c.

Moreover, to understand the effect of entropy on Li-migration in the anode materials, nudged elastic band (NEB) calculations^[103] were performed to find the energy barrier of Li⁺ ions using two different pathways: 1) top surface layer and 2) middle layer in the layered anode. During the NEB calculations, all atoms were allowed to relax, while the lattice parameters were fixed.

3. Results and Discussion

3.1. Bulk Properties

3.1.1. Structural Stability

The pristine and entropy-induced bulk HS composed of alternating layers of TiS₂ and TiSe₂ are shown in Figure 1a,b. The initial lattice parameters were chosen from the parent layered material TiSe₂^[104] which were then allowed to fully relax to obtain the structural parameters of the complete HS. The lattice parameters obtained for the TSS-HS and TSS-EI systems are listed Table 1.

These parameters are obtained without intercalating any Li-ion within the layers of the HS. The overall lattice mismatch obtained for TSS-HS and TSS-EI w.r.t. the parent material TiSe₂ lattice parameter '*a*' is 0.28% and 2.52%, respectively, which is quite low and considered within the limits of minor mismatch.^[105] In the TSS-based anode, partial substitution of Se with S leads to a reduction in atomic size and bond length due to the smaller ionic radius of S²⁻ (1.84 Å) compared to Se²⁻ (1.98 Å). This substitution results in a contraction of the lattice, particularly along the *c*-axis, thereby reducing the overall unit cell volume in TSS-HS and TSS-EI compared to pristine TiSe₂. Moreover, in TSS-EI, the substitution of Ti⁴⁺ (ionic radius 0.605 Å) with high-valent dopants, like Mo⁵⁺ (0.61 Å) and Al³⁺ (0.535 Å), introduces local lattice distortions due to differences in both ionic size and charge. While Mo⁵⁺ is comparable in size to Ti⁴⁺, its higher valence can lead to stronger Coulombic interactions and local structural tightening. Al³⁺, being significantly smaller, can cause local lattice compression. The combination of these dopants contributes to inhomogeneous lattice strain and a modest increase in the *a*-axis and unit cell volume in TSS-EI compared to TSS-HS.

Table 1. DFT calculated lattice parameters using PBE-U-D3 for TSS-HS, TSS-EI, and the reference HS material TiSe₂.

Structure	' <i>a</i> ' [Å]	' <i>c</i> ' [Å]	volume [Å ³]
TSS-HS	3.58	5.84	53.68
TSS-EI	3.66	5.87	56.47
TiSe ₂	3.57, ^[104] 3.533 ^[122]	5.995 ^[122]	69.54

Apart from low-lattice mismatch, TSS-HS was previously reported to be stable using phonon calculations, indicating that the parent HS geometry, that is, TSS-HS, is stable.^[106]

Furthermore, to identify low energy sites for Li-ions, we calculated the ground state energy of four different available intercalation sites as shown in Figure 2 (inset). The lowest energy was obtained at site-1 (i.e., at top of the Ti-site, E_1) and the energies for all other sites are provided in Figure 2 using the energy of site-1 as a reference. All other sites have relative energies, $\Delta E \gtrsim 1.0$ eV. For further calculations, site-1 was considered for Li-intercalation, and 100% Li-coverage was used for fully lithiated layered anode materials. Additionally, the formation energies of TSS-HS and TSS-EI anodes at each Li-concentration were calculated to

determine their thermodynamical stability (Figure S1, Supporting Information). It is found that formation energy of a high-entropy anode (TSS-EI) is considerably more negative than that of a conventional anode (TSS-HS) material, indicating superior thermodynamic stability. A more negative formation energy signifies a lower energy state, which corresponds to stronger chemical bonding within the material. The greater disorder inherent in materials with higher entropy contributes to this stabilization, lowering the system's overall energy and thereby improving its stability under operational conditions.

Furthermore, in order model the effect of 'enhanced-entropy' on the structural changes during cycling of the layered anode TSS-HS, the relative changes in structural parameters ' a ', ' c ' and volume were calculated (Figure 3). In Figure 3a, ' a ' exhibits a pronounced decreasing trend with lithiation (that is, charging) up to 50% Li-concentration in TSS-EI, while subsequent lithiation ($Li > 50\%$) results in a smaller reduction in ' a '. In TSS-HS, ' a ' shows a continuous, albeit somewhat erratic, shrinkage as a function of Li-concentration, which overall is greater than for the entropy-induced material. We ascribe this shrinkage to reduced intralayer repulsion between metal ions as they are reduced. The ' c ' parameter changes only slightly as a function of lithiation up to 75%, while there is a drastic reduction upon complete lithiation for both TSS-HS and TSS-EI, which is also mirrored in the volume behavior. We ascribe this shrinkage to reduced interlayer repulsion between Se and S because of Li-ion intercalation between the TiS_2 and $TiSe_2$ layers. We further note that the overall change in the ' c ' parameter and volume is less for the TSS-EI anode material.

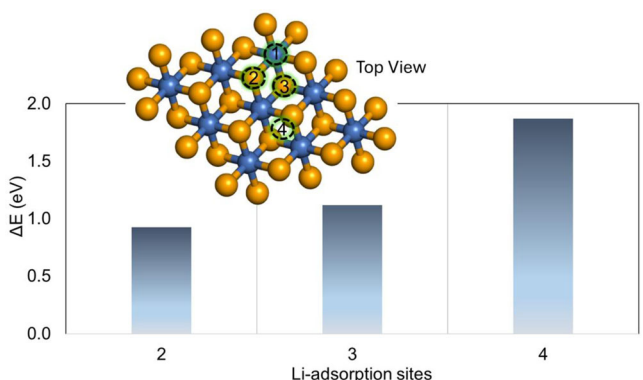


Figure 2. The difference in ground state energies of all considered sites relative to site-1. Li-intercalation sites labeled 1, 2, 3, and 4 are displayed along the ' c '-axis (inset).

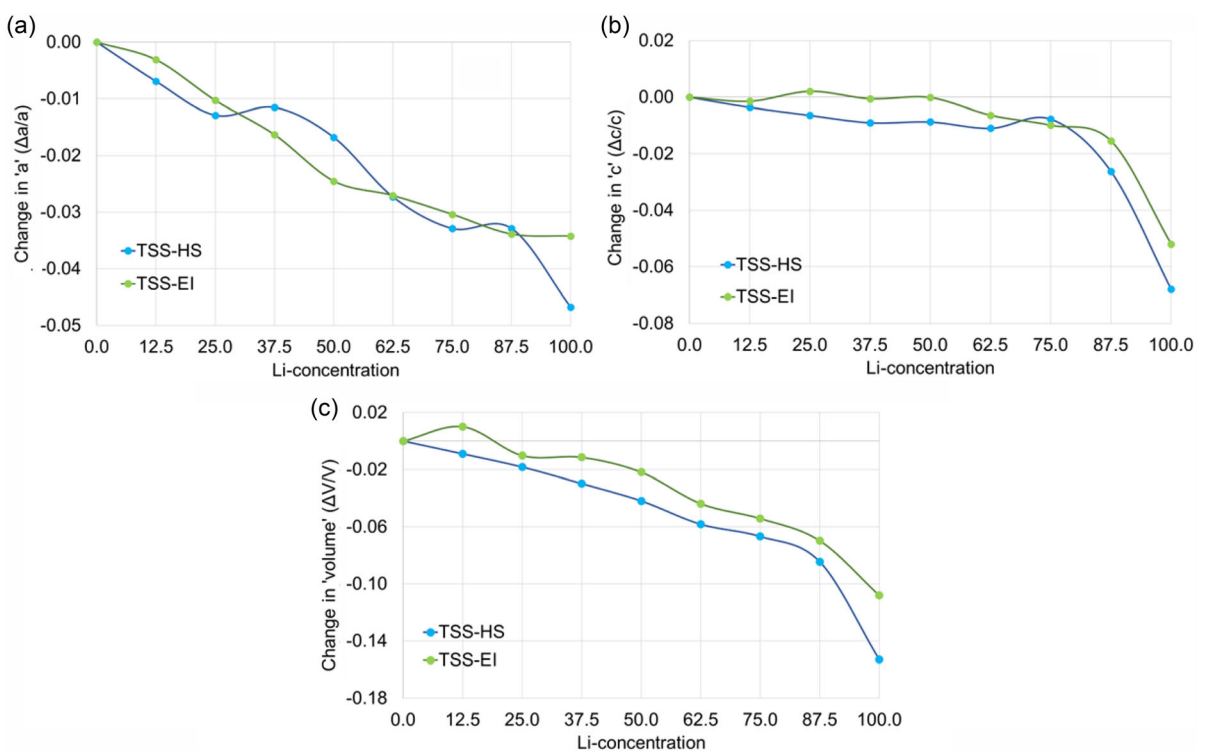


Figure 3. Relative change in a) ' a ' lattice parameter, b) ' c ' parameter, and c) volume of TSS-HS and TSS-EI as a function of Li-concentration.

Similar trends were observed in the volume change as well (Figure 3c). The change in structural parameters were further tested with larger size supercells (i.e., $5 \times 5 \times 4$) of TSS-HS and TSS-EI to test the effect of cell-size. All the lattice parameters were found consistent with the $3 \times 3 \times 2$ supercell results and quite similar structural changes were observed as a function of Li-concentration (Figure S2, Supporting Information). Suppressed structural deformation attributed to ‘entropy stabilization’ during discharging has been reported by several groups.^[54,107] Low lattice deformation may offer enhanced specific capacity as well as prolonged electrochemical cycling. Volume expansion remains a critical limitation in the design of lithium-ion battery anodes, often leading to structural degradation and poor cycling stability. For instance, commonly used materials such as $\text{Li}_{22}\text{Si}_5$ and $\text{Li}_{4.4}\text{Sn}$ exhibit substantial volume expansions of $\approx 400\%$ and 300% , respectively.^[108,109] Even graphene, known for its excellent conductivity and mechanical strength, shows a volume change of about 10%.^[110] In comparison, the TSS-HS structure demonstrates a moderate expansion of $\approx 16\%$, while our Mo-Al substituted TSS-EI anode exhibits a reduced volume change of only $\approx 11\%$. This marked reduction highlights the role of entropy introduced through cosubstitution, which helps stabilize the lattice and mitigate volumetric strain during lithiation/delithiation cycles.

3.1.2. Electronic Structure

We performed electronic structure calculations to analyze the effect of ‘entropy’ on the electronic structure and electron mobility

in TSS anode materials. Partial density of states (PDOS) obtained for HS and EI at different Li-concentrations are provided in Figure 4,5 and S3,S4, Supporting Information, respectively. Initially at Li-0%, TSS-HS contains Ti^{4+} ions which consist of zero unpaired d-electrons, thus contributing no magnetic moment. This is also observed in the Li-0% PDOS, where the spin-up and spin-down channels have identically occupied energy levels. The majority of the Ti^{4+} -d states are found in the conduction band region and there is no energy gap. Upon lithiation of TSS-HS, the Ti-ions commence redox activity, as the Ti^{4+} ions are reduced to Ti^{3+} ions, and ultimately this process is completed at the Li-100% level. We see that the Ti^{4+} -d states are shifted down in energy upon Li-insertion as these ions are being reduced. The Ti^{3+} ion have an unpaired electron, and hence, a nonzero magnetic moment is obtained for the Ti^{3+} -d states, which are located across the energy spectrum. As expected, Se-p states are observed near the Fermi level, somewhat higher than the S-p states. No significant change in the chalcogen ions electronic states is observed with lithiation in TSS-HS, suggestion no detectable anion redox. At the 100% Li-level, a band gap of ≈ 0.32 eV is observed, which may impede electron mobility in deep-charged states of the anode.

The PDOS of the entropy-induced anode TSS-EI (Figure 5, and S4, Supporting Information) shows similar trends for the $\text{Ti}^{4+} \rightarrow \text{Ti}^{3+}$ reduction with lithiation. The dopants Mo^{5+} and Al^{3+} were not found to change oxidation states during lithiation, suggesting no direct participation in redox, similar to what has been observed for cathode doping and high entropy materials.^[54,76,77,111] However, Mo^{5+} has high-spin states with nonzero magnetic

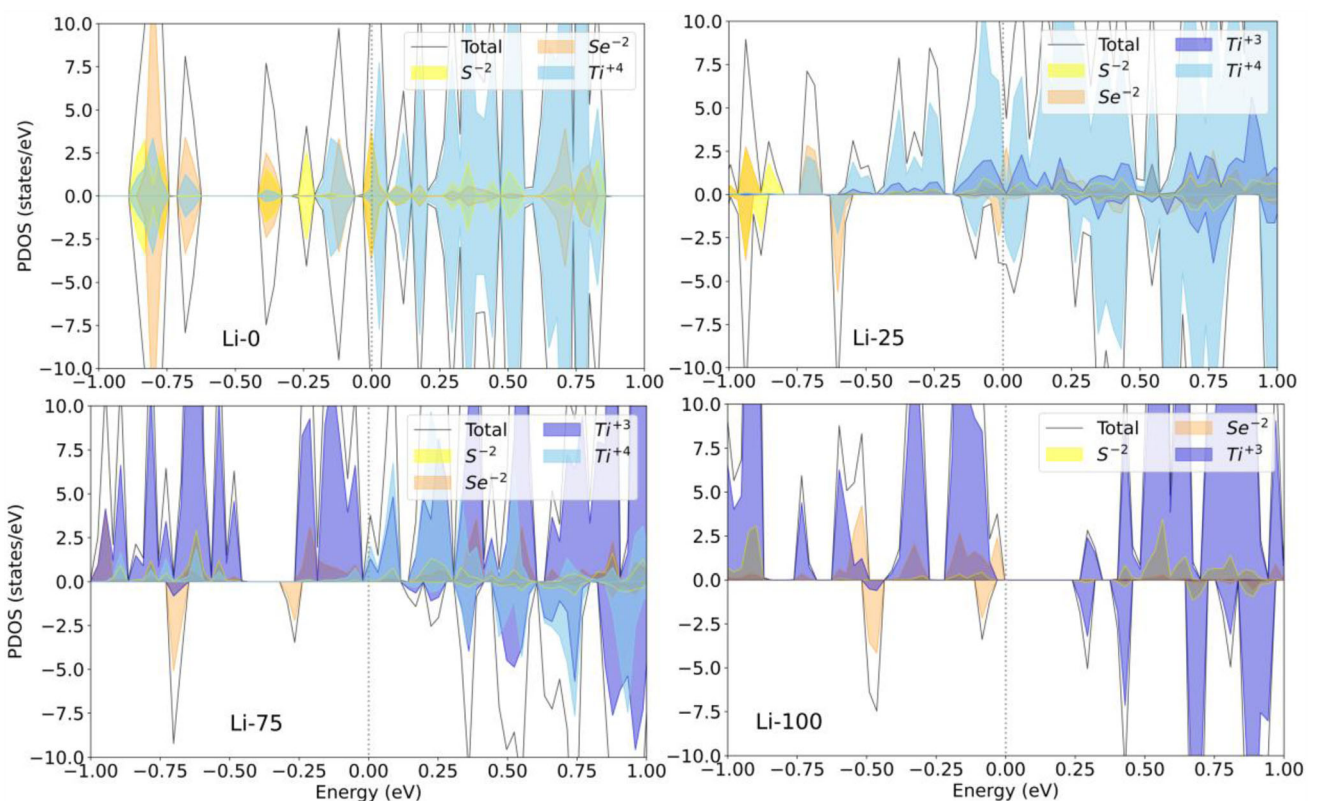


Figure 4. PDOS of TSS-HS at different Li-concentrations (Li-0 to 100%). The dotted line indicates that the Fermi level was set at 0.0 eV.

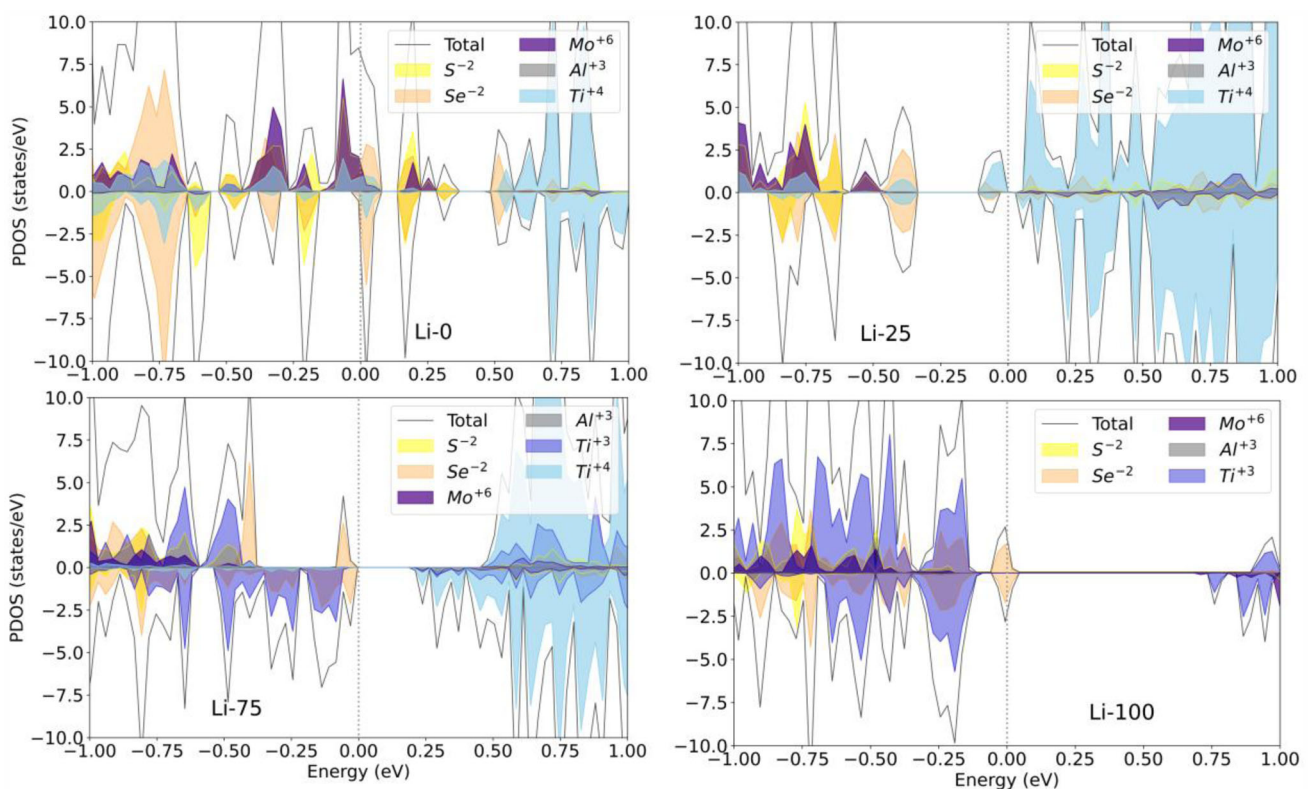


Figure 5. PDOS of TSS-EI at different Li-concentrations (Li-0 to 100%). The dotted line indicates that the Fermi level was set at 0.0 eV.

moment, whereas the electronic states of Al^{3+} are not spin polarized.

The high-valent dopant (i.e., Mo^{5+}) in TSS-EI adds conductive states into the Fermi level region, resulting in a zero bandgap at the 100% Li-level. This may offer improved electron mobility in deep-charged states resulting in better conductivity. We note that while configurational entropy plays a critical role in stabilizing the overall structure and suppressing volume strain during cycling, the zero-band gap behavior at high lithiation levels is not a direct entropic effect, but rather a consequence of dopant-induced electronic tuning.

3.1.3. Redox Activity and Bond Strength

In the PDOS analysis, we found that Ti-ions are redox active, while the chalcogen and dopant ions do not change their oxidation states during lithiation. For a closer look at the redox activity of the Ti-ions with Li-concentration, we performed redox population analysis for TSS-HS and TSS-EI anode materials. In both TSS-HS and TSS-EI pristine (discharged) states, all Ti-ions are found in a Ti^{4+} oxidation state (Figure 6). In TSS-HS, Ti^{3+} begins to appear at Li-25.0%, while in TSS-EI, Ti^{3+} emerge at Li-37.5%. The observed delay in the reduction of Ti^{4+} to Ti^{3+} in TSS-EI (starting at 37.5% Li concentration) compared to TSS-HS (at 25% Li) can be attributed to the electronic and structural role of Mo^{5+} and Al^{3+} dopants in the high-entropy framework. Mo^{5+} , being a high-valent and redox-active dopant, likely acts as an early electron acceptor during initial lithiation, thereby accommodating a portion of the inserted charge. This delays the need for charge compensation

via Ti^{4+} reduction. In essence, the presence of Mo^{5+} shifts the redox burden away from Ti, postponing its reduction to a higher Li content. Furthermore, Al^{3+} , though electrochemically inactive, contributes to local electrostatic and lattice stability, modifying the electronic environment around Ti sites and increasing the energy barrier for Ti reduction (Discussed in Section 6). In TSS-HS, all Ti^{4+} are consumed by Li-87.5%, while for TSS-EI this only occurs at Li-100.0%. Hence, the onset of Ti reduction is shifted slightly to greater lithiation levels in the TSS-EI anode material. We note that the presence of Ti^{4+} ions is important to maintain a consistent and strong bonding environment with surrounding Se and S ions. Additionally, it has been reported that Mo^{5+} and Al^{3+} ions offer strong bonding with surrounding anions which can lead to improved material stability.^[54,76,77,112]

To quantify the strength of chalcogen-metal bonds in the TSS materials, we performed integrated COHP (ICOHP) analysis, where more negative ICOHP values indicate stronger bonds. The ICOHP as a function of Li-concentration as shown in Figure 7a,b for TSS-HS and TSS-EI anode materials, respectively. From Figure 7, we observe that Ti—S and Ti—Se bonding is weakened with lithium insertion for both TSS-HS and TSS-EI, which may be attributed to $\text{Ti}^{4+} \rightarrow \text{Ti}^{3+}$ reduction. However, in Figure 7b, we see that the dopants Mo^{5+} and Al^{3+} form much stronger bonds with surrounding chalcogen ions. Stronger bonds offered by dopants Mo and Al are mainly attributed to their relatively smaller ionic radii (Mo^{5+} : 0.61 Å, Al^{3+} : 0.53 Å, Ti^{4+} : 0.60, and Ti^{3+} : 0.67 Å), which results in short, strong bonds (Figure S5, Supporting Information). This could be a factor in preventing structural deformations with lithiation in TSS-EI.

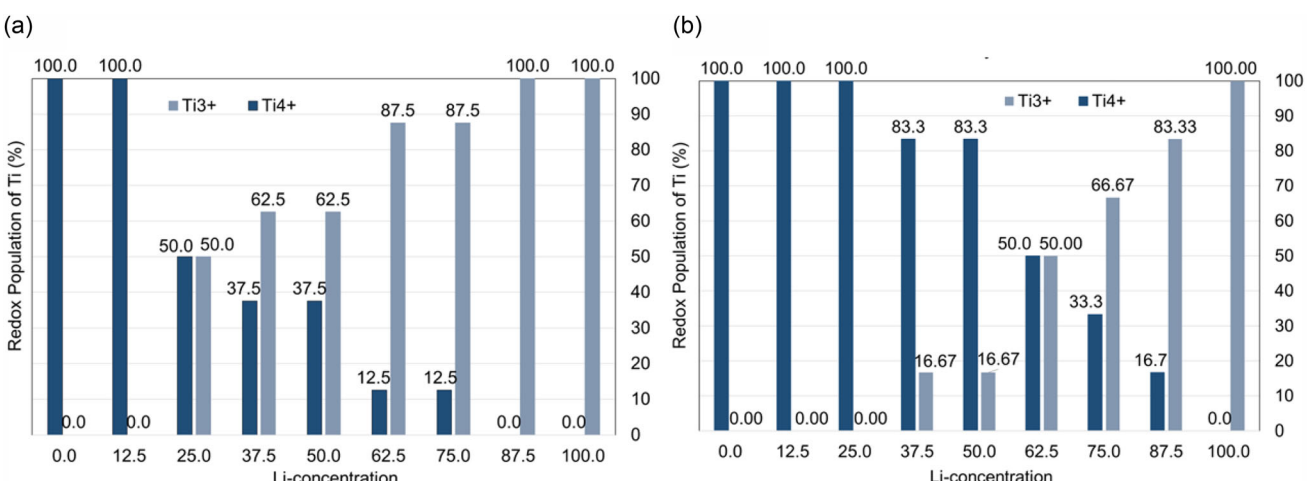


Figure 6. Redox population of Ti-ions as a function of Li-concentration in a) TSS-HS and b) TSS-EI.

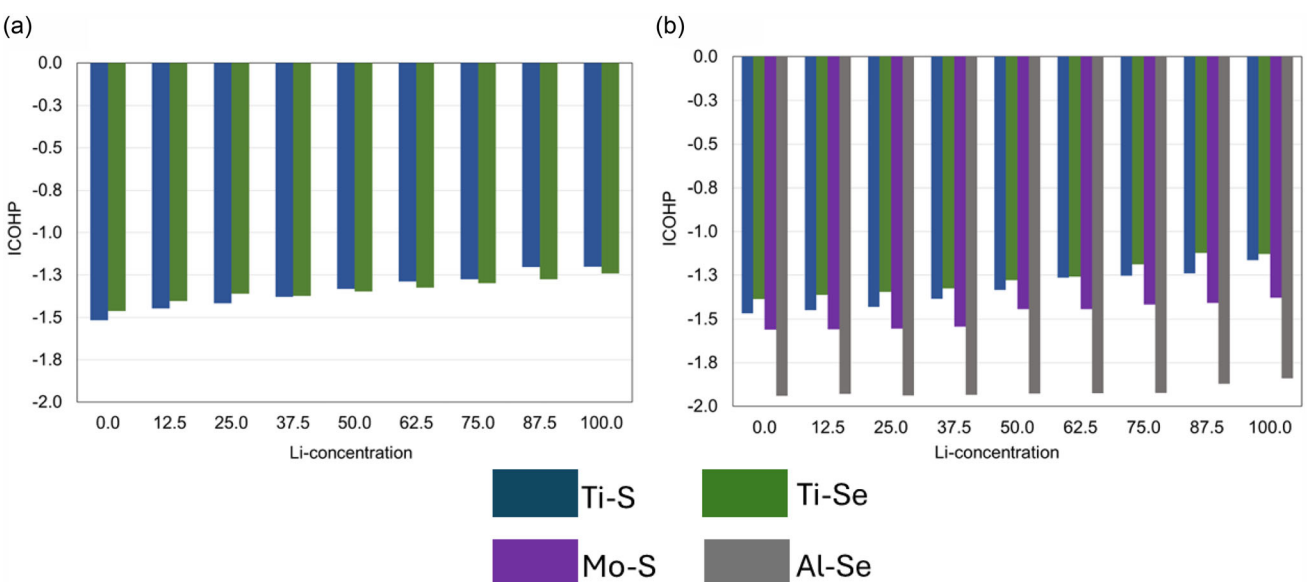


Figure 7. Metal–chalcogen ion bonding in a) TSS-HS and b) TSS-EI, showing the change in bond strength at different Li-concentration levels. Values of ICOHP (y-axis) are obtained as the ICOHP at the Fermi Level.

3.1.4. Open Circuit Voltage (OCV) Profile

In designing high-performance LIBs, OCV is a crucial factor for the development of high energy density batteries. Using Equation (2), OCV profiles (Figure 8) were obtained using the ground-state energies of TSS-EI and TSS-HS at each delithiated state.^[54] A wider operational voltage window (≈ 0.47 V) was achieved for TSS-EI compared to TSS-HS (≈ 0.40 V), which may lead to higher capacity as more Li^+ ions can be extracted with a larger voltage window. The entropy contributed widened OCV range can be ascribed to improved structural stability accompanied with suppressed volumetric strain in the TSS-EI anode. Additionally, the high potential for TSS-HS and TSS-EI are observed to be 1.28 and 1.43 V, respectively. An elevated potential enhances safety by reducing lithium plating risks.^[113]

3.2. Interphase Properties

Prior to studying the Li diffusion behavior at the EEI, the structural evolution and Li diffusion in a model electrolyte (EC, PC, and PF_6^-) was analyzed by computing the integrated radial distribution function (IRDF) (Figure 9a,b). We considered relatively short simulations^[114–116] to establish basic qualitative trends relating to ion transportation in TSS-HS and TSS-EI at the EEI. Our IRDF analyses show that Li^+ ion coordination with surrounding molecules in the electrolyte is slightly reduced in the TSS-EI–electrolyte complex (Figure 10b) compared to the TSS-HS–electrolyte (Figure 9a), with values of 1.90 to 1.33 ($\text{Li}–\text{O}$ [EC]) and 1.05 to 0.65 ($\text{Li}–\text{O}$ [PC]), respectively, within an interaction distance of 3 Å. Reduced coordination of Li ions can offer better mobility near the EEI and thus might result in better diffusion. Additionally,

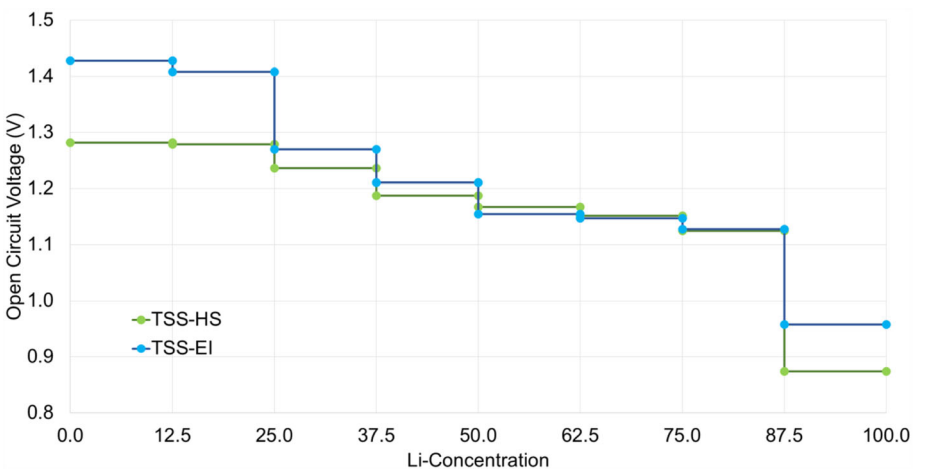


Figure 8. DFT calculated OCV versus Li-concentration for TSS-HS and TSS-EI.

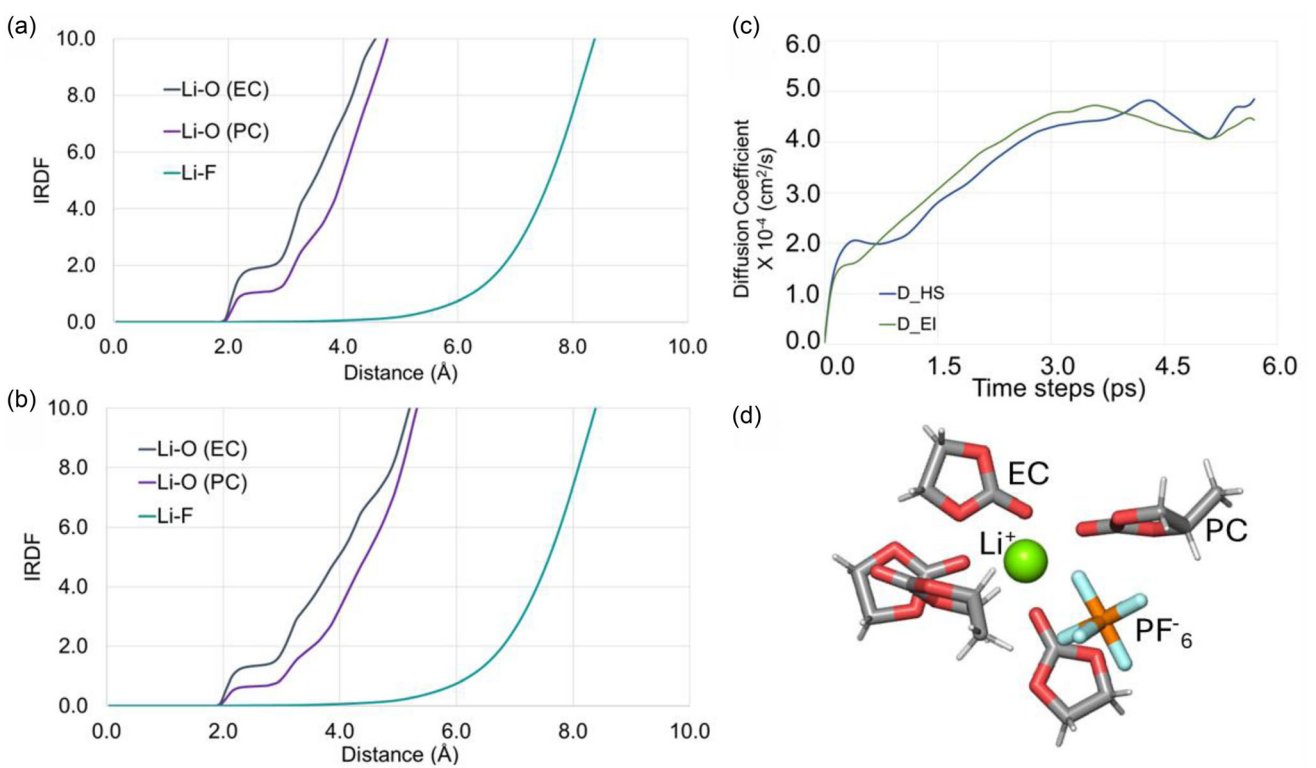


Figure 9. IRDF obtained with AIMD simulations of Li-ion and its surrounding organic solvents (EC and PC) and salt (PF_6^-) for anode materials a) TSS-HS and b) TSS-EI. c) Diffusion coefficients of Li-ions at the EEI interphase showing slightly faster diffusion at the TSS-EI:Electrolyte interphase (D_{EI}), compared to the TSS-HS:Electrolyte interphase (D_{HS}). d) Snapshot of a Li^+ ion and its surrounding electrolyte environment within a radius of 4 Å.

we can also predict from the IRDF results that the primary solvation shell at the EEI will mainly be composed of EC and PC molecules.^[117] Moreover, to gain insights into the possible composition of the EEI, pair distribution function analysis (Figure S6, Supporting Information) was carried out. Strong Li–O and Li–C peaks within 3 Å were observed for both TSS-HS and TSS-EI, indicating that EC and PC molecules dominate the primary solvation shell around Li^+ . In contrast, Li–F correlations appeared only beyond 6 Å, suggesting that PF_6^- remains spatially separated and does not directly interact with Li^+ at the interface. This

solvation structure implies that the initial EEI composition arises predominantly from solvent decomposition. The close Li^+ –solvent proximity facilitates ring-opening and breakdown of EC/PC, leading to the formation of species, such as Li_2CO_3 and lithium alkyl carbonates. Minimal Li–F interaction suggests limited LiF formation at this early stage. Therefore, the EEI on both anodes is expected to be rich in organic components with Li_2CO_3 as the dominant inorganic species.^[118–120]

The diffusion coefficients of Li ions obtained from a linear fit of the MSD using Equation (4) are shown in Figure 9c. We observe

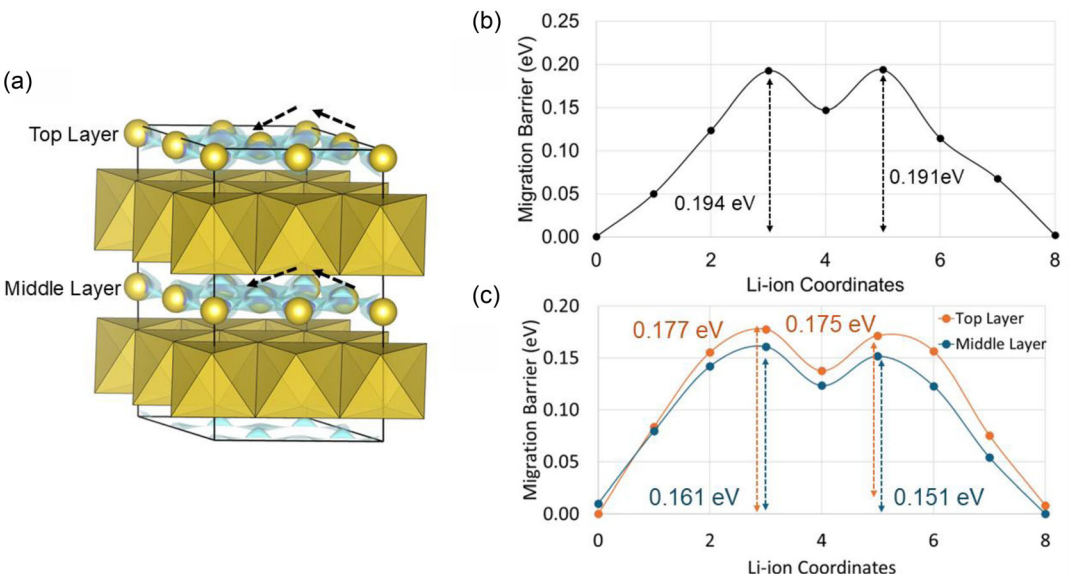


Figure 10. a) Li-migration pathways considered in top and middle layer shown with black arrows; b) and c) migration barriers of Li ion along different pathways in TSS-HS and TSS-EI, respectively.

Table 2. Computed average diffusion coefficient and ionic mobility at 300 K.

EEI	Average Diffusion Coefficient [$\times 10^{-4} \text{ cm}^2 \text{ s}^{-1}$]	Average Ionic Mobility [$\times 10^{-2} \text{ cm}^2 \text{ s V}^{-1}$]
TSS-HS: Electrolyte	4.67 ± 0.07	1.81 ± 0.03
TSS-EI: Electrolyte	5.35 ± 0.10	2.10 ± 0.08

that at the EEI with TSS-EI, there is slightly faster Li diffusion compared to EEI with TSS-HS (**Table 2**). The induced entropy introduces structural and electronic modifications in the host lattice that reduce local polarization and Li⁺ trapping, thereby facilitating smoother diffusion pathways and lowering migration barriers.

3.2.1. NEB Analysis of Li⁺ Migration Pathways

To further validate the enhanced Li⁺ transport behavior of the TSS-EI system, NEB calculations were performed to evaluate Li⁺ diffusion energy barriers along two representative migration pathways: (1) the top surface layer and (2) the middle layer within the anode structure (Figure 10). The results reveal that the TSS-EI structure exhibits significantly lower energy barriers for Li⁺ migration compared to the pristine TSS-HS system, suggesting improved ion conduction kinetics. This reduction in the diffusion barrier is primarily attributed to the increase in configurational entropy introduced by Mo–Al codoping. The presence of multiple atomic species in the host lattice leads to local compositional fluctuations and structural disorder, which in turn flatten the potential energy landscape^[121] for Li⁺ migration. Such entropy-driven lattice perturbations reduce the depth and symmetry of Li⁺ trapping sites, facilitating smoother ion transport across both surface and bulk layers. Additionally, the presence of dopants introduces subtle electronic modifications that promote charge delocalization around Li⁺ migration sites. This effect is evident

from the reduced charge accumulation on Li and Ti atoms, along with the pronounced electron affinity of Mo, as revealed by charge distribution analysis (Table S1, Supporting Information). Collectively, these factors contribute to a lower activation energy barrier for Li⁺ hopping. These combined effects highlight the role of entropy as a key enabler of fast Li⁺ diffusion in the codoped system. Together with our computed RDF, which shows weaker Li-solvent coordination, the NEB results support the conclusion that entropy-enhanced anode structures can simultaneously promote efficient desolvation and rapid solid-state diffusion—both critical for achieving high-rate performance in Li-ion batteries.

4. Conclusions

To investigate the effect of “entropy increment” on layered bulk HS anode material TSS, we performed DFT calculations of several properties relevant to electrochemistry. We performed DFT calculations of properties as a function of Li-concentration and propose that TSS-EI anode materials might experience less structural deformations, while possessing better electron mobility, bond strengths, and a wider voltage window than the low-entropy analog. Specifically, our calculations suggest that the presence of elements like Mo⁵⁺ and Al³⁺ provide reduced internal strain (less volumetric change), stronger bonds, as well as better electron mobility. We performed AIMD simulations where the IRDF, average diffusion coefficient, and average ionic mobility suggest slightly improved ion-transport for the TSS-EI anode near the EEI. Additionally, NEB calculations show reduced ion migration barriers in TSS-EI which supports faster diffusion. In summary, our work provides atomistic level insights into possible high entropy TSS anode materials for Li-ion batteries and presents ideas for future experimental work.

Acknowledgements

The author A.B. gratefully acknowledges the support of TCG CREST for providing funding that made this research possible. D.T.M. acknowledges partial support from the Israel Science Foundation (ISF) in the framework of the INREP project, INIES—the Israel National Institute of Energy Storage established by the Israel Ministry of Energy—and Israel Ministry of Energy grant no. 223-11-066.

Conflict of Interest

The authors declare no conflict of interest.

Data Availability Statement

The data that support the findings of this study are available from the corresponding author upon reasonable request.

Keywords: ab-initio molecular dynamics • density functional theory • diffusion coefficient • solid–electrolyte interphase formation • transition metal anode

- [1] B. Kang, G. Ceder, *Nature* **2009**, *458*, 190.
[2] J. M. Tarascon, M. Armand, *Nature* **2001**, *414*, 359.
[3] Q. Zhang, Y. Liu, H. Lu, D. Tang, C. Ouyang, L. Zhang, *Electrochim. Acta* **2016**, *189*, 147.
[4] G. Zhou, F. Li, H.-M. Cheng, *Energy Environ. Sci.* **2014**, *7*, 1307.
[5] L. Britnell, R. V. Gorbachev, R. Jalil, B. D. Belle, F. Schedin, A. Mishchenko, T. Georgiou, M. I. Katsnelson, L. Eaves, S. V. Morozov, N. M. R. Peres, J. Leist, A. K. Geim, K. S. Novoselov, L. A. Ponomarenko, *Science* **2012**, *335*, 947.
[6] R. Raccichini, A. Varzi, S. Passerini, B. Scrosati, *Nat. Mater.* **2015**, *14*, 271.
[7] J. E. Santos, N. M. R. Peres, J. M. B. Lopes dos Santos, A. H. Castro Neto, *Phys. Rev. B* **2011**, *84*, 085430.
[8] R. A. Nistor, M. A. Kuroda, A. A. Maarouf, G. J. Martyna, *Phys. Rev. B* **2012**, *86*, 041409.
[9] F. Guinea, M. I. Katsnelson, A. K. Geim, *Nat. Phys.* **2010**, *6*, 30.
[10] S.-M. Choi, S.-H. Jhi, Y.-W. Son, *Phys. Rev. B* **2010**, *81*, 081407.
[11] J. Lahiri, Y. Lin, P. Bozkurt, I. I. Oleynik, M. Batzill, *Nat. Nanotechnol.* **2010**, *5*, 326.
[12] K. R. Paton, E. Varlla, C. Backes, R. J. Smith, U. Khan, A. O'Neill, C. Boland, M. Lotya, O. M. Istrate, P. King, T. Higgins, S. Barwick, P. May, P. Puczkarski, I. Ahmed, M. Moebius, H. Pettersson, E. Long, J. Coelho, S. E. O'Brien, E. K. McGuire, B. M. Sanchez, G. S. Duesberg, N. McEvoy, T. J. Pennycook, C. Downing, A. Crossley, V. Nicolosi, J. N. Coleman, *Nat. Mater.* **2014**, *13*, 624.
[13] T. Georgiou, R. Jalil, B. D. Belle, L. Britnell, R. V. Gorbachev, S. V. Morozov, Y.-J. Kim, A. Gholinia, S. J. Haigh, O. Makarovskiy, L. Eaves, L. A. Ponomarenko, A. K. Geim, K. S. Novoselov, A. Mishchenko, *Nat. Nanotechnol.* **2013**, *8*, 100.
[14] B. Hunt, J. D. Sanchez-Yamagishi, A. F. Young, M. Yankowitz, B. J. LeRoy, K. Watanabe, T. Taniguchi, P. Moon, M. Koshino, P. Jarillo-Herrero, R. C. Ashoori, *Science* **2013**, *340*, 1427.
[15] X. Hong, J. Kim, S.-F. Shi, Y. Zhang, C. Jin, Y. Sun, S. Tongay, J. Wu, Y. Zhang, F. Wang, *Nat. Nanotechnol.* **2014**, *9*, 682.
[16] A. Allain, J. Kang, K. Banerjee, A. Kis, *Nat. Mater.* **2015**, *14*, 1195.
[17] T. Roy, M. Tosun, J. S. Kang, A. B. Sachid, S. B. Desai, M. Hettick, C. C. Hu, A. Javey, *ACS Nano* **2014**, *8*, 6259.
[18] F. H. L. Koppens, T. Mueller, P. Avouris, A. C. Ferrari, M. S. Vitiello, M. Polini, *Nat. Nanotechnol.* **2014**, *9*, 780.
[19] J. D. Mehew, S. Unal, E. Torres Alonso, G. F. Jones, S. Fadhil Ramadhan, M. F. Craciun, S. Russo, *Adv. Mater.* **2017**, *29*, 1700222.
[20] P. Kumar, J. Lynch, B. Song, H. Ling, F. Barrera, K. Kisslinger, H. Zhang, S. B. Anantharaman, J. Digani, H. Zhu, T. H. Choudhury, C. McAleese, X. Wang, B. R. Conran, O. Whear, M. J. Motala, M. Snure, C. Muratore, J. M. Redwing, N. R. Glavin, E. A. Stach, A. R. Davoyan, D. Jariwala, *Nat. Nanotechnol.* **2022**, *17*, 182.
[21] A. Samad, M. Noor-A-Alam, Y.-H. Shin, *J. Mat. Chem. A* **2016**, *4*, 14316.
[22] G.-C. Guo, D. Wang, X.-L. Wei, Q. Zhang, H. Liu, W.-M. Lau, L.-M. Liu, *J. Phys. Chem. Lett.* **2015**, *6*, 5002.
[23] X. Shao, K. Wang, R. Pang, X. Shi, *J. Phys. Chem. C* **2015**, *119*, 25860.
[24] G. Barik, S. Pal, *Appl. Surf. Sci.* **2022**, *596*, 153529.
[25] S. Vishwanathan, P. Chithaiah, H. S. S. R. Matte, C. N. R. Rao, *Chem. Commun.* **2024**, *60*, 1309.
[26] B. Xu, X. Ma, J. Tian, F. Zhao, Y. Liu, B. Wang, H. Yang, Y. Xia, *Ionics* **2019**, *25*, 4171.
[27] G. Du, Z. Guo, S. Wang, R. Zeng, Z. Chen, H. Liu, *Chem. Commun.* **2010**, *46*, 1106.
[28] W. Li, Y. Yang, G. Zhang, Y.-W. Zhang, *Nano Lett.* **2015**, *15*, 1691.
[29] G. A. Tritsaris, E. Kaxiras, S. Meng, E. Wang, *Nano Lett.* **2013**, *13*, 2258.
[30] Y. Li, D. Wu, Z. Zhou, C. R. Cabrera, Z. Chen, *J. Phys. Chem. Lett.* **2012**, *3*, 2221.
[31] M. Chhowalla, H. S. Shin, G. Eda, L.-J. Li, K. P. Loh, H. Zhang, *Nat. Chem.* **2013**, *5*, 263.
[32] C. J. Price, E. A. D. Baker, S. P. Hepplestone, *J. Phys. Chem. C* **2024**, *128*, 1867.
[33] D. Wang, L.-M. Liu, S.-J. Zhao, Z.-Y. Hu, H. Liu, *J. Phys. Chem. C* **2016**, *120*, 4779.
[34] Y. Yun, J. Shao, X. Shang, W. Wang, W. Huang, Q. Qu, H. Zheng, *Nanoscale Adv.* **2020**, *2*, 1878.
[35] A. J. Molina-Mendoza, E. Giovanelli, W. S. Paz, M. A. Niño, J. O. Island, C. Evangelisti, L. Aballe, M. Foerster, H. S. J. van der Zant, G. Rubio-Bollinger, N. Agrait, J. J. Palacios, E. M. Pérez, A. Castellanos-Gómez, *Nat. Commun.* **2017**, *8*, 14409.
[36] Y. Yang, S. Fang, V. Fatemi, J. Ruhman, E. Navarro-Moratalla, K. Watanabe, T. Taniguchi, E. Kaxiras, P. Jarillo-Herrero, *Phys. Rev. B* **2018**, *98*, 035203.
[37] S. Nagata, T. Aochi, T. Abe, S. Ebisu, T. Hagino, Y. Seki, K. Tsutsumi, *J. Phys. Chem. Solids* **1992**, *53*, 1259.
[38] B. Sipos, A. F. Kusmartseva, A. Akrap, H. Berger, L. Forró, E. Tutiš, *Nat. Mater.* **2008**, *7*, 960.
[39] R. Zheng, H. Yu, X. Zhang, Y. Ding, M. Xia, K. Cao, J. Shu, A. Vlad, B.-L. Su, *Angew. Chem. Int. Ed.* **2021**, *60*, 18430.
[40] D. Zhang, G. Zhao, P. Li, Y. Zhang, W. Qiu, J. Shu, Y. Jiang, S. X. Dou, W. Sun, *Chem. – A Eur. J.* **2018**, *24*, 1193.
[41] W. Li, K. Wang, S. Cheng, K. Jiang, *Adv. Energy Mater.* **2019**, *9*, 1900993.
[42] L. Wen, Y. Wu, S. Wang, J. Shi, Q. Zhang, B. Zhao, Q. Wang, C. Zhu, Z. Liu, Y. Zheng, J. Su, Y. Gao, *Nano Energy* **2022**, *93*, 106896.
[43] L. Zhang, X. Hou, K. Edström, E. J. Berg, *Batteries Supercaps* **2022**, *5*, e202200336.
[44] Z. Dong, X. Wu, M. Chen, H. Chen, K.-J. Huang, L. Wang, J. Xu, *J. Colloid. Interface Sci.* **2023**, *630*, 426.
[45] H. Liu, Z. Huang, G. Wu, Y. Wu, G. Yuan, C. He, X. Qi, J. Zhong, *J. Mat. Chem. A* **2018**, *6*, 17040.
[46] Y. Zheng, X. Kong, L. He, J. Shang, D. Wang, C. Lei, Y. Zhao, *J. Power Sources* **2023**, *580*, 233371.
[47] Q. Wang, A. Sarkar, D. Wang, L. Velasco, R. Azmi, S. S. Bhattacharya, T. Bergfeldt, A. Düvel, P. Heijmans, T. Brezesinski, H. Hahn, B. Breitung, *Energy Environ. Sci.* **2019**, *12*, 2433.
[48] Y. Ma, Y. Ma, Q. Wang, S. Schweidler, M. Botros, T. Fu, H. Hahn, T. Brezesinski, B. Breitung, *Energy Environ. Sci.* **2021**, *14*, 2883.
[49] A. Sarkar, L. Velasco, D. Wang, Q. Wang, G. Talasila, L. de Biasi, C. Kübel, T. Brezesinski, S. S. Bhattacharya, H. Hahn, B. Breitung, *Nat. Commun.* **2018**, *9*, 3400.
[50] Y. Yu, C. Yang, Y. Jiang, Z. Shang, J. Zhu, J. Zhang, M. Jiang, *Adv. Energy Mater.* **2025**, *15*, 2403086.
[51] J. Liao, S. Huang, Z. Xie, A. Wang, A. Zhu, H. Huang, W. Li, Z. He, R. Xia, Z. Wu, P. Qing, L. Chen, *Adv. Funct. Mater.* **2025**, *25*, 2506529, <https://doi.org/10.1002/adfm.202506529>.
[52] Z. Shao, L. Lin, W. Zhuang, S. Liu, P. Yang, K. Zhu, C. Li, G. Guo, W. Wang, Q. Zhang, Y. Yao, *Adv. Mater.* **2024**, *36*, 2406093.
[53] L. Lin, Z. Shao, S. Liu, P. Yang, K. Zhu, W. Zhuang, C. Li, G. Guo, W. Wang, G. Hong, B. Wu, Q. Zhang, Y. Yao, *Angew. Chem. Int. Ed.* **2025**, *64*, e202425008.
[54] A. Bano, M. Noked, D. T. Major, *Chem. Mater.* **2023**, *35*, 8426.
[55] Z. Lun, B. Ouyang, D.-H. Kwon, Y. Ha, E. E. Foley, T.-Y. Huang, Z. Cai, H. Kim, M. Balasubramanian, Y. Sun, J. Huang, Y. Tian, H. Kim, B. D. McCloskey, W. Yang, R. J. Clément, H. Ji, G. Ceder, *Nat. Mater.* **2021**, *20*, 214.
[56] W. Zheng, G. Liang, Q. Liu, J. Li, J. A. Yuwono, S. Zhang, V. K. Peterson, Z. Guo, *Joule* **2023**, *7*, 2732.
[57] O. F. Dippo, K. S. Vecchio, *Scripta Mater.* **2021**, *201*, 113974.

- [58] X. Zhao, G. Ceder, *Joule* **2022**, *6*, 2683.
- [59] S. K. Martha, J. Nanda, G. M. Veith, N. J. Dudney, *J. Power Sources* **2012**, *199*, 220.
- [60] Y. Zeng, B. Ouyang, J. Liu, Y.-W. Byeon, Z. Cai, L. J. Miara, Y. Wang, G. Ceder, *Science* **2022**, *378*, 1320.
- [61] S. Liu, Y. Yan, R. Zheng, G. Tian, X. Wang, C. Shu, *Small* **2025**, *21*, 2407855.
- [62] C. Wang, K. Wan, P. Liu, C. Zeng, S. Wang, Y. Huang, Y. Zhang, H. Xiao, C. Shu, Z. Liang, *Angew. Chem. Int. Ed.* **2025**, *64*, e202506083.
- [63] H. Lohani, A. Kumar, A. Bano, A. Ghosh, P. Kumari, A. Ahuja, A. Sengupta, D. Kumar, D. T. Major, S. Mitra, *Adv. Energy Mater.* **2024**, *14*, 2401268.
- [64] C. Wang, T. Ouyang, X. Wang, S. Liu, G. Tian, F. Fan, P. Liu, S. Wang, C. Zeng, C. Shu, *J. Energy Chem.* **2024**, *99*, 384.
- [65] Z. Yang, X. Xiang, J. Yang, Z.-Y. Zhao, *Mater. Futures* **2024**, *3*, 042103.
- [66] A. Sarkar, Q. Wang, A. Schiele, M. R. Chellali, S. S. Bhattacharya, D. Wang, T. Brezesinski, H. Hahn, L. Velasco, B. Breitung, *Adv. Mater.* **2019**, *31*, 1806236.
- [67] T. Yu, Y. Zhang, Y. Hu, K. Hu, X. Lin, G. Xie, X. Liu, K. M. Reddy, Y. Ito, H.-J. Qiu, *ACS Mater. Lett.* **2022**, *4*, 181.
- [68] P. Zhou, D. Liu, Y. Chen, M. Chen, Y. Liu, S. Chen, C. T. Kwok, Y. Tang, S. Wang, H. Pan, *J. Mater. Sci. Technol.* **2022**, *109*, 267.
- [69] Z.-X. Cai, H. Goou, Y. Ito, T. Tokunaga, M. Miyauchi, H. Abe, T. Fujita, *Chem. Sci.* **2021**, *12*, 11306.
- [70] Z. Chen, J. Wen, C. Wang, X. Kang, *Small* **2022**, *18*, 2204255.
- [71] Y. Kang, O. Cretu, J. Kikkawa, K. Kimoto, H. Nara, A. S. Nugraha, H. Kawamoto, M. Eguchi, T. Liao, Z. Sun, T. Asahi, Y. Yamauchi, *Nat. Commun.* **2023**, *14*, 4182.
- [72] X. Wang, Q. Peng, X. Zhang, X. Lv, X. Wang, Y. Fu, *J. Colloid Interface Sci.* **2022**, *607*, 1580.
- [73] H. Xu, R. Hu, Y. Zhang, H. Yan, Q. Zhu, J. Shang, S. Yang, B. Li, *Energy Storage Mater.* **2021**, *43*, 212.
- [74] Z. Qiu, Y. Li, Y. Gao, Z. Meng, Y. Sun, Y. Bai, N.-T. Suen, H.-C. Chen, Y. Pi, H. Pang, *Angew. Chem. Int. Ed.* **2023**, *62*, e202306881.
- [75] P. Zheng, J. Wu, H. Zhao, J. Li, Z. Liu, Y. Zheng, *Chem. – An Asian J.* **2025**, *20*, e202401071.
- [76] F. A. Susai, D. Kovacheva, A. Chakraborty, T. Kravchuk, R. Ravikumar, M. Talianker, J. Grinblat, L. Burstein, Y. Kauffmann, D. T. Major, B. Markovsky, D. Aurbach, *ACS Appl. Energy Mater.* **2019**, *2*, 4521.
- [77] F. A. Susai, A. Bano, S. Maiti, J. Grinblat, A. Chakraborty, H. Sclar, T. Kravchuk, A. Kondrakov, M. Tkachev, M. Talianker, D. T. Major, B. Markovsky, D. Aurbach, *J. Mater. Chem. A* **2023**, *11*, 12958.
- [78] D. J. Matthew, E. Tieu, M. D. Morse, *J. Chem. Phys.* **2017**, *146*, 144310.
- [79] J. J. Sorensen, E. Tieu, M. D. Morse, *J. Chem. Phys.* **2020**, *152*, 124305.
- [80] D. Tzeli, I. Karapetsas, D. M. Merriles, J. C. Ewigleben, M. D. Morse, *J. Phys. Chem. A* **2022**, *126*, 1168.
- [81] D. B. Keyes, *J. Chem. Educ.* **1928**, *5*, 241.
- [82] J. J. Sorensen, E. Tieu, A. Sevy, D. M. Merriles, C. Nielson, J. C. Ewigleben, M. D. Morse, *J. Phys. Chem.* **2020**, *153*, 074303.
- [83] G. Kresse, J. Hafner, *Phys. Rev. B* **1994**, *49*, 14251.
- [84] G. Kresse, J. Furthmüller, *Comput. Mater. Sci.* **1996**, *6*, 15.
- [85] P. E. Blöchl, *Phys. Rev. B* **1994**, *50*, 17953.
- [86] J. P. Perdew, K. Burke, M. Ernzerhof, *Phys. Rev. Lett.* **1996**, *77*, 3865.
- [87] S. L. Dudarev, G. A. Botton, S. Y. Savrasov, C. J. Humphreys, A. P. Sutton, *Phys. Rev. B* **1998**, *57*, 1505.
- [88] Z. Zhang, B. Hong, M. Yi, X. Fan, Z. Zhang, X. Huang, Y. Lai, *Chem. Eng. J.* **2022**, *445*, 136825.
- [89] S. Grimme, *J. Comput. Chem.* **2004**, *25*, 1463.
- [90] S. Maintz, V. L. Deringer, A. L. Tchougréeff, R. Dronskowski, *J. Comput. Chem.* **2016**, *37*, 1030.
- [91] S. Maintz, V. L. Deringer, A. L. Tchougréeff, R. Dronskowski, *J. Comput. Chem.* **2013**, *34*, 2557.
- [92] R. Dronskowski, P. E. Bloechl, *J. Phys. Chem.* **1993**, *97*, 8617.
- [93] V. L. Deringer, A. L. Tchougréeff, R. Dronskowski, *J. Phys. Chem. A* **2011**, *115*, 5461.
- [94] A. Urban, D.-H. Seo, G. Ceder, *npj Comput. Mater.* **2016**, *2*, 16002.
- [95] M. S. Islam, C. A. J. Fisher, *Chem. Soc. Rev.* **2014**, *43*, 185.
- [96] A. Chakraborty, S. Kunnikuruvan, S. Kumar, B. Markovsky, D. Aurbach, M. Dixit, D. T. Major, *Chem. Mater.* **2020**, *32*, 915.
- [97] M. Ebadi, D. Brandell, C. M. Araujo, *J. Chem. Phys.* **2016**, *145*.
- [98] E. P. Kamphaus, S. Angarita-Gomez, X. Qin, M. Shao, M. Engelhard, K. T. Mueller, V. Murugesan, P. B. Balbuena, *ACS Appl. Mater. Interfaces* **2019**, *11*, 31467.
- [99] S. Zhao, Y. Zhang, W. J. Weber, *J. Phys. Chem. C* **2017**, *121*, 26622.
- [100] T. Chakraborty, A. Hens, S. Kulashrestha, N. Chandra Murmu, P. Banerjee, *Phys. E* **2015**, *69*, 371.
- [101] D. E. Galvez-Aranda, J. M. Seminario, *J. Electrochem. Soc.* **2019**, *166*, A2048.
- [102] L. Martínez, R. Andrade, E. G. Birgin, J. M. Martínez, *J. Comput. Chem.* **2009**, *30*, 2157.
- [103] G. Henkelman, B. P. Uberuaga, H. Jónsson, *J. Chem. Phys.* **2000**, *113*, 9901.
- [104] A. Bano, D. T. Major, *Appl. Phys. Lett.* **2023**, *122*, 182403.
- [105] Y. Lu, J. Chen, M. J. Coupin, S. Sinha, J. H. Warner, *Adv. Mater.* **2022**, *34*, 2205403.
- [106] N. A. Pike, A. Dewandre, F. Chaltin, L. Garcia Gonzalez, S. Pillitteri, T. Ratz, M. J. Verstraete, *Phys. Rev. B* **2021**, *103*, 235307.
- [107] R. Zhang, C. Wang, P. Zou, R. Lin, L. Ma, L. Yin, T. Li, W. Xu, H. Jia, Q. Li, S. Sainio, K. Kisslinger, S. E. Trask, S. N. Ehrlich, Y. Yang, A. M. Kiss, M. Ge, B. J. Polzin, S. J. Lee, W. Xu, Y. Ren, H. L. Xin, *Nature* **2022**, *610*, 67.
- [108] H. Mou, W. Xiao, C. Miao, R. Li, L. Yu, *Front. Chem.* **2020**, *8*, <https://doi.org/10.3389/fchem.2020.00141>.
- [109] U. Kasavajjula, C. Wang, A. J. Appleby, *J. Power Sources* **2007**, *163*, 1003.
- [110] Z.-S. Wu, W. Ren, L. Xu, F. Li, H.-M. Cheng, *ACS Nano* **2011**, *5*, 5463.
- [111] H. H. Sun, U.-H. Kim, J.-H. Park, S.-W. Park, D.-H. Seo, A. Heller, C. B. Mullins, C. S. Yoon, Y.-K. Sun, *Nat. Commun.* **2021**, *12*, 6552.
- [112] M. Dixit, B. Markovsky, D. Aurbach, D. T. Major, *J. Electrochem. Soc.* **2017**, *164*, A6359.
- [113] S. P. Rangarajan, Y. Barsukov, P. P. Mukherjee, *J. Mater. Chem. A* **2020**, *8*, 13077.
- [114] A. Bafecky, M. Naseri, M. Faraji, M. M. Fadlallah, D. M. Hoat, H. R. Jappor, M. Ghergherehchi, D. Gogova, H. Afarideh, *Sci. Rep.* **2022**, *12*, 22269.
- [115] M. Singh, B. Chakraborty, *Phys. Chem. Chem. Phys.* **2023**, *25*, 16018.
- [116] S. S. R. Yamijala, *J. Phys. Chem. C* **2019**, *123*, 25113.
- [117] Z. Luo, S. A. Burrows, S. K. Smoukov, X. Fan, E. S. Boek, *J. Phys. Chem. B* **2023**, *127*, 2224.
- [118] S. Hwang, D.-H. Kim, J. H. Shin, J. E. Jang, K. H. Ahn, C. Lee, H. Lee, *J. Phys. Chem. C* **2018**, *122*, 19438.
- [119] K. Leung, *Phys. Chem. Chem. Phys.* **2015**, *17*, 1637.
- [120] K. Xu, *Chem. Rev.* **2014**, *114*, 11503.
- [121] Z. Wang, S. Qiao, M. Ma, T. Li, H. K. Liu, S. X. Dou, S. Chong, *ACS Nano* **2025**, *19*, 15148.
- [122] P. Chen, Y. H. Chan, X. Y. Fang, Y. Zhang, M. Y. Chou, S. K. Mo, Z. Hussain, A. V. Fedorov, T. C. Chiang, *Nat. Commun.* **2015**, *6*, 8943.

Manuscript received: April 21, 2025

Revised manuscript received: June 20, 2025

Version of record online: